Biogeosciences
Discussions

Open Access

EGU

Longitudinal contrast in Turbulence along a ∼19S section in the Pacific and its consequences on biogeochemical fluxes

Pascale Bouruet-Aubertot[1], Yannis Cuypers[1], Andrea Doglioli[2], Mathieu Caffin[2], Christophe Yohia[2], Alain de Verneil[2], Anne Petrenko[2], Dominique Lefèvre[2], Hervé Le Goff[1], Gilles Rougier[2], Marc Picheral[3], and Thierry Moutin[2]

[1]Sorbonne Université- UPMC Univ. Paris 06- LOCEAN, France
[2] Aix Marseille Univ, Université de Toulon, CNRS, IRD, MIO UM 110 , 13288, Marseille, France
[3] LOV, Villefranche sur mer, France

Correspondence: P. Bouruet-Aubertot (pascale.bouruet-aubertot@upmc.fr)

Abstract. Microstructure measurements were performed along the OUTPACE longitudinal transect in the tropical Pacific (Moutin and Bonnet, 2015). Small-scale dynamics and three-dimensional turbulence in the first 800m surface layer were characterized based on hydrographic and current measurements at fine scale and turbulence measurements at cm scale using a vertical microstructure profiler. The possible impact of turbulence on biogeochemical budgets in the surface layer was also

5   addressed in this region of increasing oligotrophy to the East. The dissipation rate of turbulent kinetic energy, ϵ, showed an interesting contrast along the longitudinal transect with higher turbulence level in the West, i.e. the Melanesian Archipelago, compared to the East, within the South Pacific Subtropical Gyre. The surface layer with enhanced turbulence decreased in vertical extent traveling eastward. This spatial pattern was correlated to the energy level of the internal wave field, higher in the West compared to the East. The difference in wave energy mostly resulted from enhanced wind power input into inertial

10   motions in the West. Moreover, three long duration stations were sampled along the cruise transect, each over three inertial periods. The analysis from the western long duration station gave evidence of an energetic baroclinic near-inertial wave that was responsible for the enhanced ϵ. This was in strong contrast with the observations at the two eastern long duration stations where semi-diurnal internal tides dominate. Averaged nitrate turbulent diffusive fluxes were at least twice as large at the western station than at the two eastern stations due to the higher vertical diffusion coefficient. In the surface layer, above the nitracline,

15   phosphate turbulent diffusive fluxes were significant except at the very eastern part of the transect. This input may have an important role in sustaining the development of N_2-fixing organisms that were evidenced as the main primary contributors to the biological pump in the area. The time-space intermittency of mixing events, intrinsic to turbulence, was underlined but its consequences on micro-organisms would deserve a dedicated study.

Copyright statement.

1 Introduction

The subtropical South Pacific is one of the main oceanic deserts characterized by an increasing oligotrophy to the East. A 43-day long cruise, the OUTPACE experiment, was performed in this region, along an $\sim 19S$ longitudinal transect, during the 2015 austral summer in order to characterize the biological pump and its coupling with dynamical processes (Moutin et al.,

5 2017). In addition to the trophic gradient the OUTPACE transect is also characterized by a longitudinal contrast in dynamics between the 'energetic' Melanesian Archipelago (MA) and the 'quiet' South Pacific Subtropical Gyre (SPSG) (e.g., Rousselet et al., 2017). Hence the OUTPACE experiment provides a unique opportunity to focus on physical and biological interactions (e.g., Rousselet et al., 2017) that may prove crucial in understanding biological pump functionning (e.g., Guidi et al., 2012; Ascani et al., 2013). The influence of the mesoscale and submesoscale circulations on the spatial distribution and transport was

10 detailed by Rousselet et al. (2017). In particular they showed the strong impact of fronts on the spatial distribution of bacteria and phytoplancton. A detailed study of an anomalous surface bloom event by de Verneil et al. (2017) revealed instead the main impact of mesoscale advection. At smaller-scales three dimensional turbulence may have a strong impact on the biological pump through the input of nutrients into the euphotic layer and more generally in enhancing, in the stratified ocean, vertical transports through turbulent diffusion (e.g., Ledwell et al., 2008). The level of turbulence is almost unknown in the OUTPACE

15 area. To our knowledge, the only microstructure measurements were performed in the western part of the subtropical South Pacific during the Malaspina expedition (Fernández-Castro et al., 2014, 2015) as part of an extensive microstructure survey in the tropical and subtropical oceans. For the leg done in the OUTPACE region, the averaged ϵ in the stratified $\sim 300m$ below the mixed layer was $\sim 10^{-8} \, Wkg^{-1}$, well above the typical background dissipation rate for open ocean. Indirect estimates of ϵ based on ARGO floats data fall in the same range as Fernández-Castro et al. (2014) as shown by Whalen et al. (2012).

20 This study based on the global scale ARGO floats dataset also revealed that the South subtropical Pacific is one of the most undersampled area. At the larger scale of the South Pacific ocean, the equatorial zone is well-known as a hotspot for turbulence where shear instability prevails as a result of the strongly sheared current system (e.g., Gregg et al., 1985; Sun et al., 1998; Richards et al., 2015). At subtropical latitudes, where the background shear is lower, internal waves are expected to play a major role on the onset of turbulence in the stratified interior. Global maps of the energy flux into near-inertial motions show

25 enhanced semi-diurnal tide energy conversion in the western part of the subtropical South Pacific while the annual mean energy flux into inertial motions is enhanced at mid-latitudes as well as around a SE oriented track from the Equator to 40S and within $\sim 180 - 200E$ longitude (Alford and Zhao, 2007, Fig.9). The latter process is subject to seasonal variations especially in subtropical regions where the generation of energetic baroclinic near-inertial waves is favored during the cyclone season (e.g., Liu et al., 2008).

30 The contribution of the biological pump in the OUTPACE region to the main C, N and P biogeochemical cycles was one of the main purpose of the OUTPACE project (Moutin et al., 2017). Moutin et al. (submitted, this issue) built a first-order budget at daily scale of these main elements while Caffin et al. (submitted, this issue) focused on the role of N2 fixation. N2 fixation was evidenced as the dominant process involved in the N cycle in regions where trichodesmium dominate. The input of nitrate through turbulent diffusion was found of negligible contribution in the euphotic layer as a result of a very deep nitracline. This

rose the question of the available source of other nutrients in the euphotic layer able to sustain the development of N_2-fixing organisms, the main primary contributors to the biological pump in the area (Caffin et al., submitted, this issue).

The purpose of this paper is to characterize three-dimensional turbulence along the OUTPACE transect with microstructure measurements performed at both one-day short duration stations and at long duration stations lasting three inertial periods. The

5 idea is also to provide insights on the main mechanisms responsible for the observed turbulence with a focus on long duration stations that allow a characterization of the internal wave field. How these small-scale dynamics influences biogeochemical fluxes is another issue that is eventually addressed.

2 Data and methods

The OUTPACE cruise took place in early 2015 from February 18th to April 3rd onboard the french oceanographic research

10 vessel l'Atalante (Moutin et al., 2017). A set of 15 short duration stations (SD) over 24h as well as 3 long duration stations (LD) over three inertial periods were performed along an almost zonal transect starting from west of New Caledonia and ending near Tahiti (Fig. 1).

2.1 CTD and LADCP

Conductivity-Temperature-Depth (CTD) measurements were performed on a rosette using a SeaBird SBE 9plus instrument.

15 Data were averaged over 1-m bins to filter out spurious salinity peaks using Sea-Bird electronics software. Simultaneously, currents were measured from a 300 kHz RDI Lowered broadband acoustic Doppler current profiler (LADCP). LADCP data were processed using the Visbeck inversion method and provided vertical profiles of horizontal currents at 8 m resolution. In addition the ship was equipped with two SADCPs, RDI Ocean Surveyors with frequencies 150kHz and 75kHz yielding to processed currents averaged over 2min time interval and with vertical bins of 8m and 24m respectively.

20 ### 2.2 Microstructure measurements with VMP1000

Microstructure measurements were collected using a vertical microstructure profiler, 'VMP1000' (Rockland Scientific). This tethered profiler was equipped with microstructure sensors, two shear sensors and one temprature sensor, as well as with Sea-Bird temperature and conductivity sensors and a high frequency fluorometer. A total number of 123 profiles were performed with repeated profiles at LD stations and a few profiles at each SD station (Table 1). The dissipation rate of turbulent kinetic

25 energy (ϵ) was inferred from centimeter-scale shear measurements. The vertical wavenumber shear spectrum was computed within the inertial range, typically within meter to centimeter scales. The experimental spectrum was next compared to the empirical spectrum, the Nasmyth spectrum (Nasmyth, 1970), which allowed to validate the estimate of ϵ (e.g., Ferron et al., 2014). ϵ was computed over a $1m$ depth interval, then a $8m$ moving average was applied on this signal. The estimated noise level is of $5 \times 10^{-11} W kg^{-1}$.

2.3 Diffusivity estimates

The diapycnal diffusivity, K_z, is commonly inferred from the kinetic energy dissipation rate using the Osborn (1980) relationship:

$$K_z = \Gamma \epsilon N^{-2} \tag{1}$$

5   where Γ is a mixing efficiency defined as the ratio between the buoyancy flux and the dissipation rate, $\Gamma = -\frac{g}{\rho_0} \frac{\overline{\rho' w'}}{\epsilon}$ with w' and ρ' the vertical velocity and density fluctuations, and N the buoyancy frequency, inferred from the sorted density profile in order to avoid spurious negative values associated with overturns, $N = \sqrt{-\frac{g}{\rho_0} \frac{d\rho_{sorted}}{dz}}$, with a $8-m$ moving average then applied on this signal. Γ was generally set to 0.2 until the recent findings by Shih et al. (2005) and Bouffard and Boegman (2013). These authors found a decrease of Γ for increasing turbulence intensity, I, defined as:

10    $$I = \epsilon / (\nu N^2) \tag{2}$$

where ν is the molecular viscosity. In term of timescales, I is the ratio of the square of the Kolmogorov time scale, namely the dissipation time scale of eddies at the Kolmogorov scale ($\sqrt{\nu/\epsilon}$), and the buoyancy time scale ($1/N$). Shih et al. (2005) showed in a numerical study that the Osborn relationship overestimated K_z when $I > 100$ and proposed a new parameterization of K_z for this regime. A few years later Bouffard and Boegman (2013) proposed a refined parameterization of K_z including in-situ microstructure measurements in lakes as well. They defined different regimes with the following formulations for K_z:

- $K_z = 10^{-7} m^2 s^{-1}$ within the diffusive sub-regime, $I < 1.7$

- $K_z = \frac{0.1}{7^{1/4}} \nu I^{3/2}$ within the buoyancy controlled sub-regime, I within $[1.7; 8.5]$

- $K_z = 0.2\nu I$, i.e. the Osborn relationship within the intermediate regime, I within $[8.5, 400]$

- $K_z = 4\nu I^{1/2}$ within the energetic regime, $I > 400$

20   with $\nu = 1.2 \times 10^{-6} m^2 s^{-1}$. Note that for the OUTPACE datatset where most I values are smaller than 100, the K_z values inferred from the Bouffard and Boegman parameterization that is applied here do not differ signficantly from those inferred from the Osborn relationship.

3 Spatial pattern of turbulence

An overview of the spatial pattern of turbulence is given with depth-averaged values of ϵ and K_z below the mixed layer at each
25   station (Fig.1). Depth-averaged dissipation rates, $<\epsilon>$, vary within an order of magnitude within $[10^{-9.5}; 10^{-8.5}] Wkg^{-1}$. The highest values are observed West of 185, in the shallower part, while the lowest values are observed East of 185, in the deeper part. The same contrast is retrieved on $<K_z>$ with values ranging within $[10^{-5.8}; 10^{-4.8}] m^2 s^{-1}$. The western part of our study area which shows the highest turbulence level is also the region where the most intense velocities are observed

as illustrated with altimetry-derived currents produced by AVISO along the RV l'Atalante cruise path (Fig.2a). The vertical section of the total velocity modulus inferred from the SADCP data shows that this contrast is also observed at depth with slightly larger velocities in the western part of our study area (Figure 2b). There the bathymetry ranges typically from 4000m up to a few hundred meters locally with significant topographic slopes, which is consistent with the higher velocity signal; by

5   comparison, in the East the bathymetry is almost flat with $\sim 5000m$ depth. More insights on turbulence are given with vertical sections of ϵ and K_z in Figure 3a and b. The range of ϵ values covers 3 orders of magnitude, typically below the mixed layer down to 300m depth, and presents a typical patchy pattern with spots of intense turbulence with values up to $\sim 10^{-8} W kg^{-1}$ down to 500m. Most of these events are observed in the West and their occurence decreases eastward and downward (Fig.3a). The K_z pattern presents an even stronger contrast between the western and eastern parts of our study area as a result of the

10 combination of smaller ϵ and larger N in the eastern part. To gain further insights on the origin of this contrast in turbulence, the possible occurrence of shear instability is addressed with buoyancy frequency, N, shear, S and Richardson number, Ri, sections displayed in Figure 4. The stratification is strong in the first 100m with a pycnocline that is generally well marked except in the western part of the transect westward of 165 and around 180 and 188 longitudes. The shear is significantly higher west of 190 with high values over the full vertical extent of the measurements in the West as well as within a mid

15 longitudinal region, $[\sim 180; \sim 190]$, that is coincident with a weaker surface stratification around 180 longitude (Fig. 4a and b). Shear instability is more likely to occur west of 190 where most of the subcritical Ri are observed which suggests that it is responsible for the enhanced dissipation observed there (Fig3 and 4c). The possible impact of internal waves was estimated indirectly through the two main energy sources for these waves, namely tidal forcing and wind power input (Fig.5 and 6). The depth-integrated tidal generation force is displayed in Figure 5 for the $K1$ and $M2$ constituents. There is a strong similarity

20 between the two constituents with a generation that is favoured in the western part of our study area which is shallower and with stronger topographic gradients than the eastern part of our study area. The most western region is characterized by numerous spots of generation with a depth-integrated generation force of $10^3 m^2 s^{-2}$ while eastward of 170 longitude there is only one main generation site around longitude 180 (Fig5a). This spatial distribution of the internal tide forcing might suggest a similar contrast in the internal tide induced dissipation since the high modes responsible of turbulence are expected to dissipate within

25 a few tens of kms of the generation site (e.g., St Laurent et al., 2002). Maps of wind power input on inertial motions, also referred to as inertial flux, were computed using the spectral method described by Alford (2003). The wind stress data were inferred from WRF numerical simulations (Klemp et al., 2007; Skamarock et al., 2005) and the seasonal climatology was used for the mixed layer depth. The power input into inertial motions gives insights on the generation of baroclinic near-inertial waves (niw) at the base of the mixed layer through inertial pumping (e.g., Gill, 1984). The maps reveal a striking longitudinal

30 contrast in inertial flux until mid March (Fig.6a-e). The strongest wind power input was observed in the western part of our study area. This is consistent with the climatology of storms and cyclones in the area that are typically formed in the SW tropical Pacific (e.g. Diamond et al., 2013). At the beginning of the cruise the largest power input was localized SW of the cruise stations (Fig6a). Later a major event was observed (Fig6d) during the passage of a tropical cyclone over the area while the RV l'Atalante was sampling to the East. Eventually by the end of the cruise the inertial flux was small over the OUTPACE

35 region with one spot of weak inertial flux observed in the East (Fig6f-g). These maps suggest that energetic niw are likely to be

generated in the western part of our study area prior to the cruise and until mid-March (Fig6a-b). The first event of large inertial flux prior to the cruise may be particularly insightfull since it is likely to lead to the generation of equatorward propagation niw within the OUTPACE sampling area, a scenario which is consistent with large ϵ values there (Fig.1).

4 Possible impact of internal waves: focus on long duration stations

5   Three long duration stations were sampled each over three inertial periods, LD-A in the western part of the transect and LD-B and LD-C in the eastern part of the transect (see Table 1 and Fig.1). Turbulence at LD-A is by far the largest down to 400m depth with contrasted mean ϵ and K_z between LD-A on one hand and LD-B and LD-C on the other hand (Fig7a and b), within a factor of $5-10$ for ϵ and K_z. Possible occurrence of shear instability is examined by comparing mean profiles of shear square, S^2, and N^2 (Fig.7c). While the mean stratification is fairly close at the three stations the shear is far larger at LD-A compared
10   to LD-B and LD-C within a factor of 10 within $[50m, 200m]$ (Fig.7c). Furthermore within $[100m, 200m]$ S^2 is larger than N^2 at LD-A pointing out possible shear instability. This depth range coincides with local ϵ maxima thus reinforcing the shear instability hypothesis.

We next focused on the characterization of the internal wave field that may reinforce the vertical shear and contribute to the onset of turbulence. Currents magnitude at LD-A is the largest (Fig8a and b), of the order of $0.4ms^{-1}$. Detailed insights
15   from the 150kHz SADCP reveal a wavy pattern with two frequencies clearly identified (Fig8a): strong upward propagating bands close to the inertial period, of about 1.5 day, and the semi-diurnal period, which manifests itself through semi-diurnal heaving of upward propagation niw bands. The former is observed over the first two hundred meters only while the latter is observed down to $\sim 800m$ depth (Fig.8a and b). The weaker currents at LD-B and LD-C are comparable with maximum amplitude of $0.2ms^{-1}$ (Fig8c-f). Periodic motions are also evidenced with inertial oscillations in the first few meters (Fig8c)
20   and a combination of near-inertial and tidal periods at depth. Noticeably an upward phase propagation of niw can be inferred at LD-B from the 38kHz SADCP data (Fig8d). At LD-C the semi-diurnal tidal signal dominates (Fig8f). The dominance of niw at LD-A is consistent with the highest wind power input inertial motions at LD-A (Fig9g) compared to LD-B and LD-C (Fig9h and i). Instead the contrast observed between the semi-diurnal depth-integrated generating force at LD-A compared to that at LD-B and LD-C (Fig9d and e-f) is not evidenced on the semi-diurnal currents (Fig8). This is well evidenced below $\sim 300m$
25   depth where the semi-diurnal tidal signal dominates at all stations (Fig8b, d and f). This difference might result from localized generation areas of small scales that are not predicted by the estimate performed with low resolution fields (tidal model and bathymetry) or from low modes with long range propagation.

Figure 10 summarizes the main characteristics of the three long duration stations. The enhanced ϵ at LD-A is correlated with an energetic niw (Fig.10a). The significant decrease in ϵ, coincident with a sharp shutdown of the near-inertial baroclinic signal
30   around 250m, shows the main effect of niw on dissipation. This transition is associated with a strong variation in the subinertial flow that suggests a wave mean flow interaction (e.g. critical level). LD-B and LD-C present strong similarities in ϵ and niw and M2 kinetic energies. The local maxima in near-inertial kinetic energy may evidence niw beams. The semi-diurnal kinetic energy presents an interesting contrast between LD-B and LD-C: while it is larger at LD-B in the first 500m and smaller below

the opposite is observed at LD-C with maximum semi-diurnal energy below 500m depth. The subinertial flow is the weakest at LD-C (Fig.10c) while the low-frequency flow at LD-B presents weak vertical variations (Fig.10b), both features suggesting a weak influence on internal wave propagation. The subinertial flow is by far the largest at LD-A down to $\sim 250m$ (Fig.10a). The contrast in turbulence between the three stations is mostly confined in the upper few hundred meters as a result of an energetic

5 niw and its interaction with the strongly sheared subinertial flow. Deeper, variations in ϵ and kinetic energies are much weaker and of the same order of magnitude at the three stations.

5 Impact of turbulence on biogeochemical fluxes: spatial pattern and intermittency

The fluorescence along the OUTPACE transect is typical of a transition from an oligotrophic area in the MA toward an ultraoligotrophic area in the SPSG (e.g., Moutin et al., 2017) with a deepening of the deep chlorophyll maximum, DCM, from

10 $\sim 60m$ to $\sim 160m$ (Fig.11a). There is one noticeable exception to this trend with a near surface fluorescence maximum at $\sim 35m$ depth, at LD-B. de Verneil et al. (2017), who focused on the characterization of this anomalous event, explained its occurrence by the main impact of mesoscale advection. The deepening of the DCM results from that of the nitracline, an evolution consistent with the increasing oligotrophy to the East (Fig.11a). The turbulent diffusive nitrate flux displays the same longitudinal trend (Fig.11c). Large variations are noted, that result from the strong variability of K_z (Fig.11b). The nitrate

15 turbulent diffusive flux averaged within a 20m layer around the DCM varies within one order of magnitude (not shown). The phosphate turbulent diffusive flux displays the similar longitudinal gradient but, as opposed to the nitrate turbulent diffusive flux, displays non zero values above the DCM, in the first $\sim$20-80-m surface layer (Fig.11d). Phosphate turbulent diffusive flux is in average smaller than the nitrate turbulent diffusive flux but its relative impact may be rescaled in terms of the N/P Redfield ratio, of the order of $1/16$. Hence, for visual comparison between the two fluxes, the scale for the phosphate turbulent

20 diffusive fluxes differs from that of the nitrate turbulent diffusive flux within the Redfield ratio in Figures 11 and followings. This striking difference in phosphate and nitrate turbulent diffusive fluxes within the euphotic layer may play an important role on the development of micro-organisms as discussed later.

Turbulent diffusive fluxes of nitrate and phosphate were further analyzed at long duration stations (Fig12). The time-depth evolution of K_z underlines the very large values encountered at the most turbulent station, LD-A, in contrast with values at LD-

25 B and LD-C that show the occurrence of a few spots of intense mixing in a more quiescent background with $K_z \sim 10^{-6} \, m^2 s^{-1}$ (Fig12a, d and g). The largest nitrate and phosphate turbulent diffusive fluxes occur at LD-A (Fig12b) while the smallest values are observed at LD-C (Fig12h). Phosphate turbuelnt diffusive fluxes are significant well above the DCM at LD-A and LD-B (Fig12b and e). Various spots of large phosphate turbulent diffusive fluxes are also evidenced in the first $\sim$20-80-m that can be correlated with events of intense turbulence (Fig12b, e and d). At LD-C the only event of significant phosphate turbulent

30 diffusive flux results from a strong turbulent event (Fig12h). The input of nitrate through turbulent diffusion into the euphotic layer was characterized by the nitrate turbulent diffusive flux at the nitracline. The large range of variations of the nitrate turbulent diffusive flux is illustrated with histograms at the LD stations (Fig.13). A density interval of $3 \times 10^{-2} \, kg \, m^{-3}$ around the isopycnal that corresponds to the top of the nitracline is chosen for its relevance regarding the input into the euphotic layer.

The mean nitrate turbulent diffusive flux is by far larger at LD-A with a large range of variation of about 2 orders of magnitude (Fig.13b). This results from the distribution of K_z values over 2 orders of magnitude that presents a bimodal distribution with moderate values associated with the 'background state' and large values associated with intense turbulent events related to the near-inertial baroclinic wave (e.g. Fig8a). The distribution of the nitrate turbulent diffusive flux is fairly similar at LD-
5 B and LD-C with one main peak (Fig13d and f). The average value is however quite different with an average value twice higher at LD-C than at LD-B. This results from a more pronounced nitracline at LD-C since the K_z distributions do not differ significantly at the two stations with averaged values of $3 \times 10^{-6}\, m^2 s^{-1}$ and $2.7 \times 10^{-6}\, m^2 s^{-1}$ respectively (Fig13c and e). In the Melanesian Archipelago, the input of nitrate into the photic layer is of negligible contribution during the stratified period (Caffin et al., submitted, this issue) and on an annual time scale (Moutin et al., submitted, this issue) compared to the input of
10 N by N2 fixation. The low and deep turbulent nitrate turbulent diffusive fluxes (Fig.11c) may not explain the higher primary production and N2 fixation rates observed in the upper 0-40 m (Moutin et al., submitted, this issue, their figs 6a and 6b). New production (Dugdale and Goering, 1967) is mainly supported by N_2-fixing organisms and phosphate may appear as the ultimate control of N input by N2 fixation in this area (Moutin et al., 2008). The concentration of phosphate is not as strongly limited as that of nitrate in the euphotic layer with significant turbulent diffusive flux locally, especially around 170 and 190
15 longitudes (Fig.11d). Therefore, local phosphate turbulent diffusive fluxes may contribute to sustain new primary production. Figure 14 summarizes the contrast between long duration station in the surface layer with histograms of K_z, phosphate and nitrate turbulent diffusive fluxes within $[20m-80m]$. As in the previous figures the scale for the nitrate and phosphate turbulent diffusive fluxes match with the Redfield ratio for visual comparison of the relative impact of each of these fluxes on micro-organisms. Significant nitrate turbulent diffusive flux is observed at LD-A as opposed to the LD-B and LD-C as a result of
20 shallower nitracline (Fig.14c, f and i), the most extreme case being that of LD-C with zero nitrate turbulent diffusive flux (Fig.14i). The station average of the phosphate turbulent diffusive flux varies within an order of magnitude eastward, from LD-A to LD-C (Fig.14b, e and h). While at LD-A the phosphate turbulent diffusive flux is of the same order of magnitude as that of the nitrate turbulent diffusive flux at LD-A (Fig.14b and c) there is at least an order of magnitude difference between phosphate and nitrate turbulent diffusive fluxes at LD-B (Fig.14e and f). The significant values of the phosphate turbulent diffusive flux
25 observed there suggests an impact on micro-organisms (Fig.14e) as opposed to the case of LD-C that displays the smallest values (Fig.14h). Low nitrogen fixation rates were measured in the gyre at LD-C, probably because of iron depletion (Bonnet et al., 2017) and this may explain why relatively high phosphate concentrations were measured there in the upper layer with relatively low turbulent diffusive fluxes of phosphate.

6 Conclusions

30 Variations within a factor of 10 of the depth-integrated ϵ were observed along the OUTPACE transect. The largest ϵ observed in the West compare well with the few measurements performed by Fernández-Castro et al. (2014, 2015) in the area during the Malaspina expedition. The range of values is comparable with 80% of ϵ values within $[6 \times 10^{-10}; 10^{-8}]\, W kg^{-1}$ in the first 300m below the mixed layer for the Malaspina expedition and 82% for the OUTPACE ϵ within $[30m, 300m]$ west of 180

longitude. Shear instability was evidenced as one main process responsible for turbulence which is a well-known mechanism in the strongly sheared Pacific equatorial currents (e.g. Richards et al., 2015). Richards et al. (2012) also mentioned the modulation of the turbulence level over a 3 year period with different ENSO states in the western equatorial Pacific, with a maximum shear during La Niña events compared to El Niño events. How this turbulence cycle is relevant to the OUTPACE region would be an

5 interesting point to address to check with possible higher turbulence level provided that the OUTPACE cruise took place during an El Niño event. Shear instability was found more likely to occur in the western part of our study area with most critical Ri encountered there. This basic analysis thus explained the contrast in dissipation observed along the transect. The main forcings of internal waves were found to vary significantly along the 19S longitudinal transect thus pointing out the possible impact of internal wave on the contrast in energy dissipation. The most striking factor was related to the atmospheric forcing with the

10 occurrence of cyclones in the West leading to an energetic baroclinic near-inertial wave field. This internal wave component was characterized at the western long duration station, LD-A, as well as its impact on energy dissipation. These scenarios are typically encountered in tropical regions where baroclinic near-inertial waves are known to contribute to energy dissipation in the upper ocean (e.g., Cuypers et al., 2013; Soares and Richards, 2013). The process of dissipation is often constrained by the mean subinertial flow with ray focusing or critical levels depending on the spatial structure of the flow (e.g., Whitt and

15 Thomas, 2013; Soares et al., 2014). These mechanisms were not addressed here but will be the focus of a future study using observations at the LD-A site.

The impact of turbulence on biogeochemical fluxes was estimated based on nitrate and phosphate turbulent diffusive fluxes. The decrease of these fluxes eastward was found to be consistent with the increasing oligotrophy. As a result of a deep nitracline (e.g., Moutin et al., submitted, this issue; Caffin et al., submitted, this issue) the nitrate input into the euphotic layer through

20 turbulent diffusion was found to provide only a subordinate contribution to the N budget with a $1-8\%$ contribution to the new N (Caffin et al., submitted, this issue). The input of phosphate in the surface layer was also addressed as a possible source for sustaining the development of N_2-fixing organisms. Phosphate turbulent diffusive fluxes mean values were significant in the euphotic layer with the exception of the most eastern station. In all cases, a few events of large fluxes driven by localized intense turbulent events were identified. The large variations in the turbulent diffusive fluxes resulting from the occurrence

25 of strong turbulent events were thus underlined with a focus on long duration stations (see also Caffin et al., submitted, this issue). This rose the question of the estimate of the turbulent input of nitrate in the euphotic layer when establishing C, N and P budgets as well as the impact of turbulence intermittency on micro-organisms (e.g., Liccardo et al., 2013).

Competing interests.

Disclaimer.

References

Alford, M. H., 2003: Improved global maps and 54-year history of wind-work on ocean inertial motions. *Geophysical Research Letters*, **30 (8)**.

Alford, M. H. and Z. Zhao, 2007: Global patterns of low-mode internal-wave propagation. part ii: Group velocity. *Journal of physical oceanography*, **37 (7)**, 1849–1858.

Ascani, F., K. J. Richards, E. Firing, S. Grant, K. S. Johnson, Y. Jia, R. Lukas, and D. M. Karl, 2013: Physical and biological controls of nitrate concentrations in the upper subtropical North Pacific Ocean. *Deep Sea Research Part II: Topical Studies in Oceanography*, **93**, 119–134.

Bonnet, S., M. Caffin, H. Berthelot, and T. Moutin, 2017: Hot spot of N2 fixation in the western tropical south pacific pleads for a spatial decoupling between N2 fixation and denitrification. *Proceedings of the National Academy of Sciences*, **114 (14)**, E2800–E2801.

Bouffard, D. and L. Boegman, 2013: A diapycnal diffusivity model for stratified environmental flows. *Dynamics of Atmospheres and Oceans*, **61**, 14–34.

Caffin, M., et al., submitted, this issue: Nitrogen budgets following a lagrangian strategy in the western tropical South Pacific Ocean: the prominent role of N2 fixation (outpace cruise). *Biogeosciences*, **14 (13)**, 3207.

Cuypers, Y., X. Le Vaillant, P. Bouruet-Aubertot, J. Vialard, and M. J. Mcphaden, 2013: Tropical storm-induced near-inertial internal waves during the cirene experiment: Energy fluxes and impact on vertical mixing. *Journal of Geophysical Research: Oceans*, **118 (1)**, 358–380.

de Verneil, A., L. Rousselet, A. Doglioli, A. Petrenko, and T. Moutin, 2017: The fate of a southwest pacific bloom: gauging the impact of submesoscale vs. mesoscale circulation on biological gradients in the subtropics. *Biogeosciences*, **14**, 3471–3486.

Diamond, H. J., A. M. Lorrey, and J. A. Renwick, 2013: A southwest Pacific tropical cyclone climatology and linkages to the El Niño–Southern Oscillation. *Journal of Climate*, **26 (1)**, 3–25.

Dugdale, R. and J. Goering, 1967: Uptake of new and regenerated forms of nitrogen in primary productivity. *Limnology and oceanography*, **12 (2)**, 196–206.

Fernández-Castro, B., B. Mouriño-Carballido, V. Benítez-Barrios, P. Chouciño, E. Fraile-Nuez, R. Graña, M. Piedeleu, and A. Rodríguez-Santana, 2014: Microstructure turbulence and diffusivity parameterization in the tropical and subtropical Atlantic, Pacific and Indian Oceans during the Malaspina 2010 expedition. *Deep Sea Research Part I: Oceanographic Research Papers*, **94**, 15–30.

Fernández-Castro, B., et al., 2015: Importance of salt fingering for new nitrogen supply in the oligotrophic ocean. *Nature communications*, **6**, doi:10.1038/ncomms9002.

Ferron, B., F. Kokoszka, H. Mercier, and P. Lherminier, 2014: Dissipation rate estimates from microstructure and finescale internal wave observations along the A25 Greenland-Portugal OVIDE line. *Journal of Atmospheric and Oceanic Technology*, **31**, 2530–2543.

Gill, A., 1984: On the behavior of internal waves in the wakes of storms. *Journal of Physical Oceanography*, **14 (7)**, 1129–1151.

Gregg, M., H. Peters, J. Wesson, N. Oakey, and T. Shay, 1985: Intensive measurements of turbulence and shear in the equatorial undercurrent. *Nature*, **318 (6042)**, 140.

Guidi, L., et al., 2012: Does eddy-eddy interaction control surface phytoplankton distribution and carbon export in the north pacific subtropical gyre? *Journal of Geophysical Research: Biogeosciences*, **117 (G02024, doi:10.129/2012JG001984)**.

Klemp, J. B., W. C. Skamarock, and J. Dudhia, 2007: Conservative split-explicit time integration methods for the compressible nonhydrostatic equations. *Monthly Weather Review*, **135 (8)**, 2897–2913.

Ledwell, J. R., D. J. McGillicuddy Jr, and L. A. Anderson, 2008: Nutrient flux into an intense deep chlorophyll layer in a mode-water eddy. *Deep Sea Research Part II: Topical Studies in Oceanography*, **55 (10-13)**, 1139–1160.

Liccardo, A., A. Fierro, D. Iudicone, P. Bouruet-Aubertot, and L. Dubroca, 2013: Response of the deep chlorophyll maximum to fluctuations in vertical mixing intensity. *Progress in oceanography*, **109**, 33–46.

Liu, L. L., W. Wang, and R. X. Huang, 2008: The mechanical energy input to the ocean induced by tropical cyclones. *Journal of Physical Oceanography*, **38 (6)**, 1253–1266.

Moutin, T. and S. Bonnet, 2015: Outpace cruise, rv l'atalante. doi:10.17600/15000900 pp.

Moutin, T., A. M. Doglioli, A. de Verneil, and S. Bonnet, 2017: Preface: The Oligotrophy to the UlTra-oligotrophy PACific Experiment (OUTPACE cruise, 18 February to 3 April 2015). *Biogeosciences Discuss.*, **14 (13)**, 3207–3220.

Moutin, T., D. M. Karl, S. Duhamel, P. Rimmelin, P. Raimbault, B. A. Van Mooy, and H. Claustre, 2008: Phosphate availability and the ultimate control of new nitrogen input by nitrogen fixation in the tropical Pacific Ocean. *Biogeosciences Discussions*, **5**, 95–109.

Moutin, T., et al., submitted, this issue: Nutrient availability and the ultimate control of the biological carbon pump in the western tropical south Pacific Ocean.

Nasmyth, P. W., 1970: Oceanic turbulence. *University of British Columbia*.

Osborn, T., 1980: Estimates of the local rate of vertical diffusion from dissipation measurements. *Journal of Physical Oceanography*, **10 (1)**, 83–89.

Richards, K., Y. Kashino, A. Natarov, and E. Firing, 2012: Mixing in the western equatorial Pacific and its modulation by ENSO. *Geophysical Research Letters*, **39 (2)**, L02 604.

Richards, K., et al., 2015: Shear-generated turbulence in the equatorial Pacific produced by small vertical scale flow features. *Journal of Geophysical Research: Oceans*, **120 (5)**, 3777–3791.

Rousselet, L., A. De Verneil, A. M. Doglioli, A. A. Petrenko, S. Duhamel, C. Maes, and B. Blanke, 2017: Large to submesoscale surface circulation and its implications on biogeochemical/biological horizontal distributions during the outpace cruise (southwest pacific). *Biogeosciences Discussions*, doi:10.5194/bg–2017–456.

Shih, L. H., J. R. Koseff, G. N. Ivey, and J. H. Ferziger, 2005: Parameterization of turbulent fluxes and scales using homogeneous sheared stably stratified turbulence simulations. *Journal of Fluid Mechanics*, **525**, 193–214.

Skamarock, W. C., et al., 2005: A description of the advanced research WRF version 2. *NCAR Tech. Note*.

Soares, S. and K. Richards, 2013: Radiation of inertial kinetic energy as near-inertial waves forced by tropical Pacific Easterly waves. *Geophysical Research Letters*, **40 (9)**, 1760–1765.

Soares, S. M., K. J. Richards, and A. Natarov, 2014: Near inertial waves in the tropical Indian Ocean: Energy fluxes and dissipation. *American Geophysical Union, Ocean Sciences Mtg., Honolulu HI*.

St Laurent, L., H. Simmons, and S. Jayne, 2002: Estimating tidally driven mixing in the deep ocean. *Geophysical research letters*, **29 (23)**, 2106–2109.

Sun, C., W. D. Smyth, and J. N. Moum, 1998: Dynamic instability of stratified shear flow in the upper equatorial Pacific. *Journal of Geophysical Research: Oceans*, **103 (C5)**, 10 323–10 337.

Whalen, C., L. Talley, and J. MacKinnon, 2012: Spatial and temporal variability of global ocean mixing inferred from argo profiles. *Geophysical Research Letters*, **39 (18)**, L18 612.

Whitt, D. B. and L. N. Thomas, 2013: Near-inertial waves in strongly baroclinic currents. *Journal of Physical Oceanography*, **43 (4)**, 706–725.

Biogeosciences
Discussions

Open Access
EGU

List of Figures

## List of Tables

Figure 1. Log values of dissipation rate of turbulent kinetic energy ($W\,kg^{-1}$) (a) and vertical diffusion coefficient (b) averaged below the mixed layer depth, over $100m - 800m$ (log scale). Bathymetry is shown with gray color scale (ETOPO1 1 arc minute- Amante, C. and B.W. Eakins, 2009. ETOPO1 1 Arc-Minute Global Relief Model: Procedures, Data Sources and Analysis. NOAA Technical Memorandum NESDIS NGDC-24. National Geophysical Data Center, NOAA. doi:10.7289/V5C8276M). Time-averaged values at long duration stations, LD-A, LD-B and LD-C are displayed with diamonds while values at short duration stations are displayed with circles.
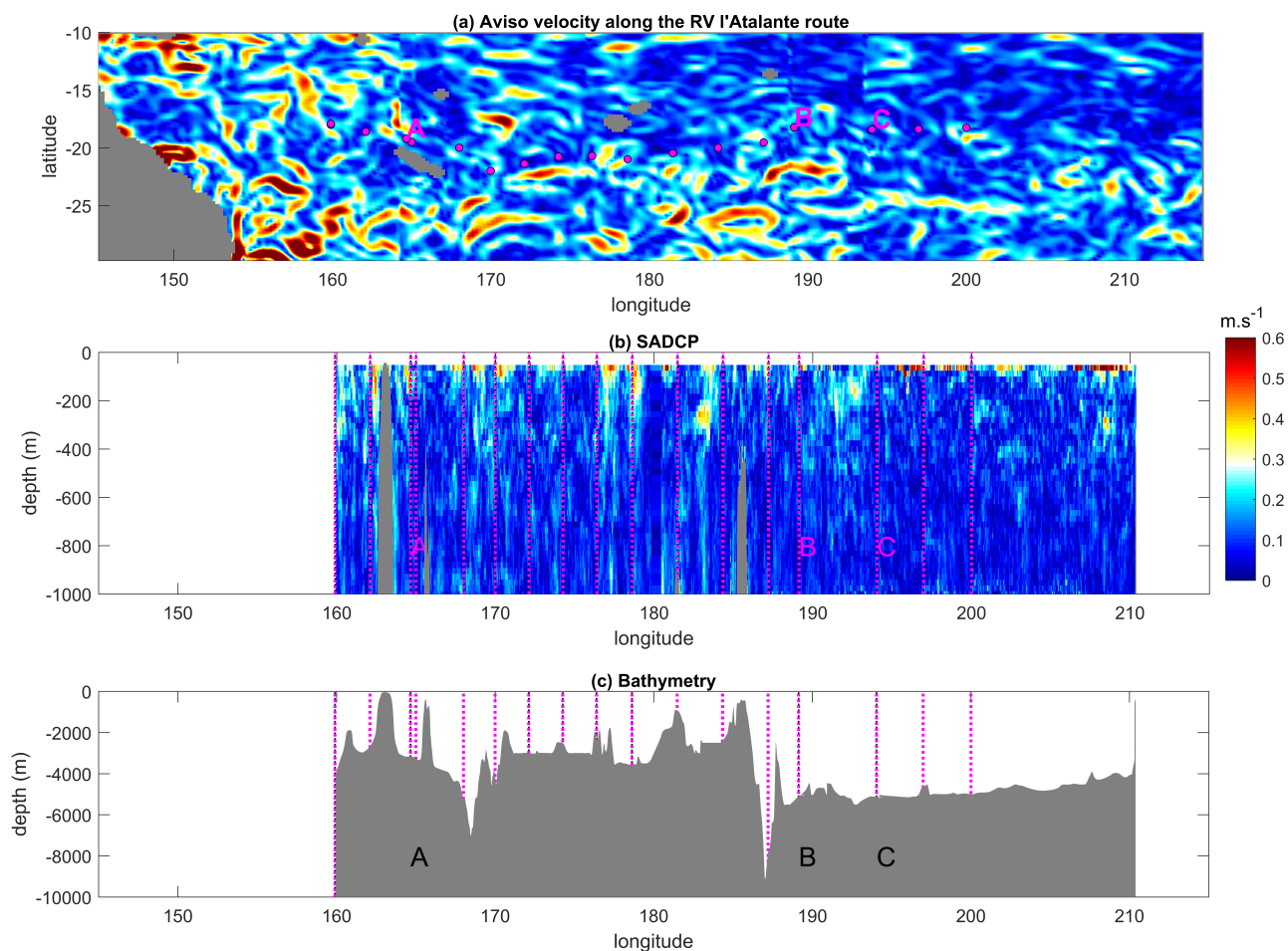
Figure 2. Surface geostrophic currents inferred from AVISO altimetric data, (a); longitude-depth section of 38kHz SADCP velocity modulus, (b); bathymetry along the RV l'Atalante route, (c); VMP stations are displayed with magenta circles in (a) and with vertical dashed magental lines in (b) and (c).
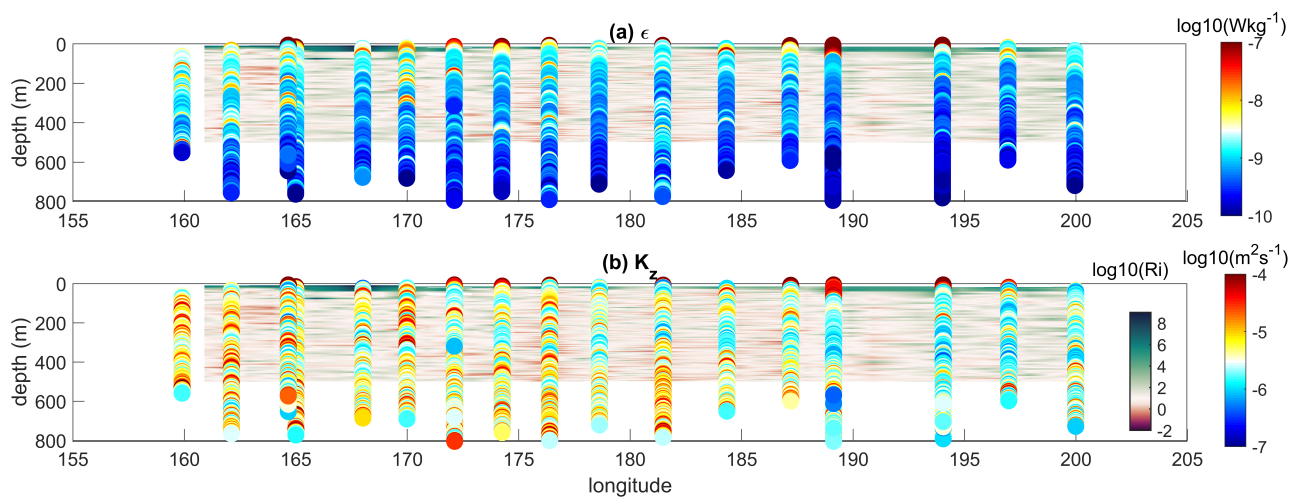
Figure 3. Log values of dissipation rate of turbulent kinetic energy ($W\,kg^{-1}$) (a) and vertical diffusion coefficient ($m^2\,s^{-1}$) (b) with log values of Ri in background colorscale.
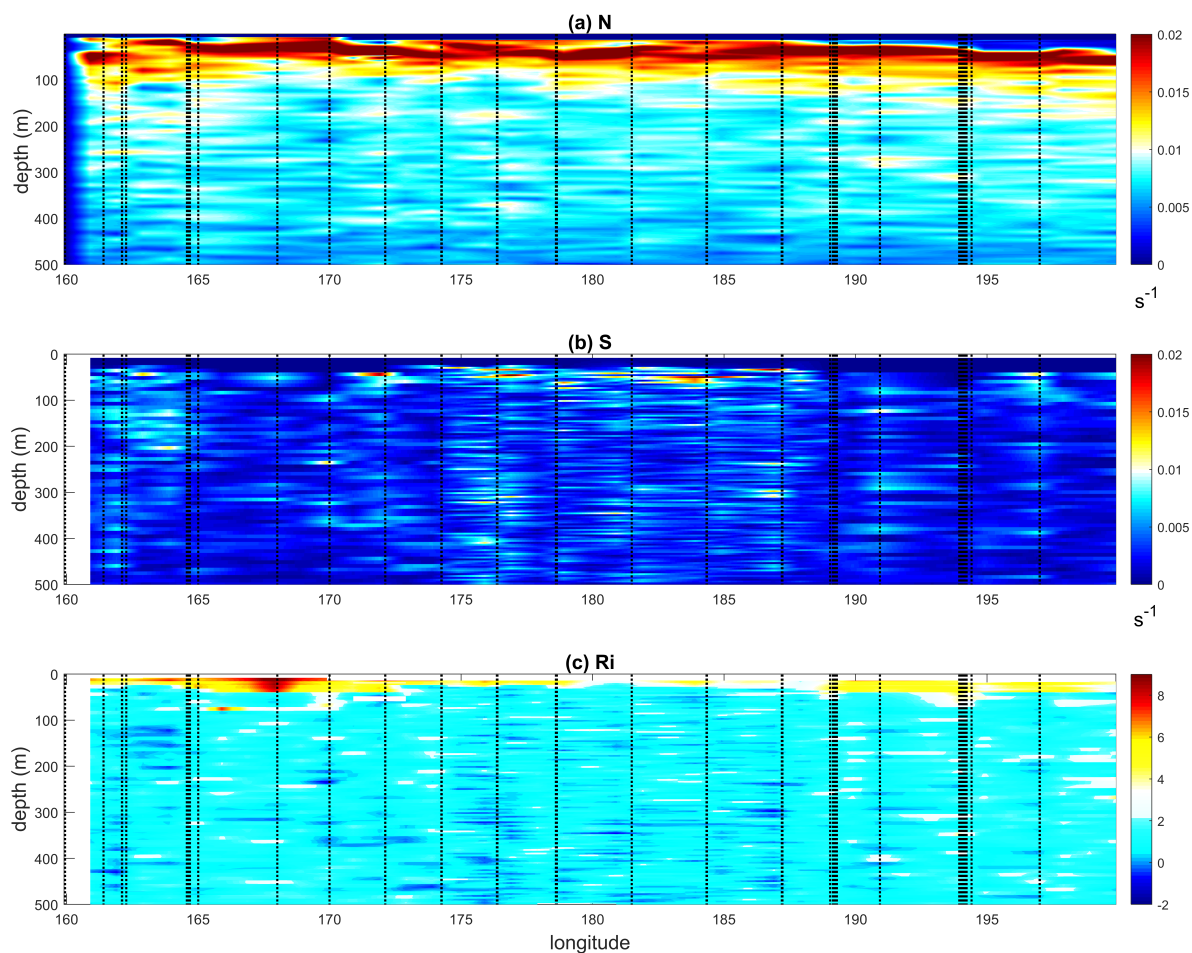
Figure 4. Buoyancy frequency, N, (a), shear, S, (b) and Richardson number, Ri, (c) as a function of longitude and depth. The location of the CTD profiles is displayed with black dashed lines.
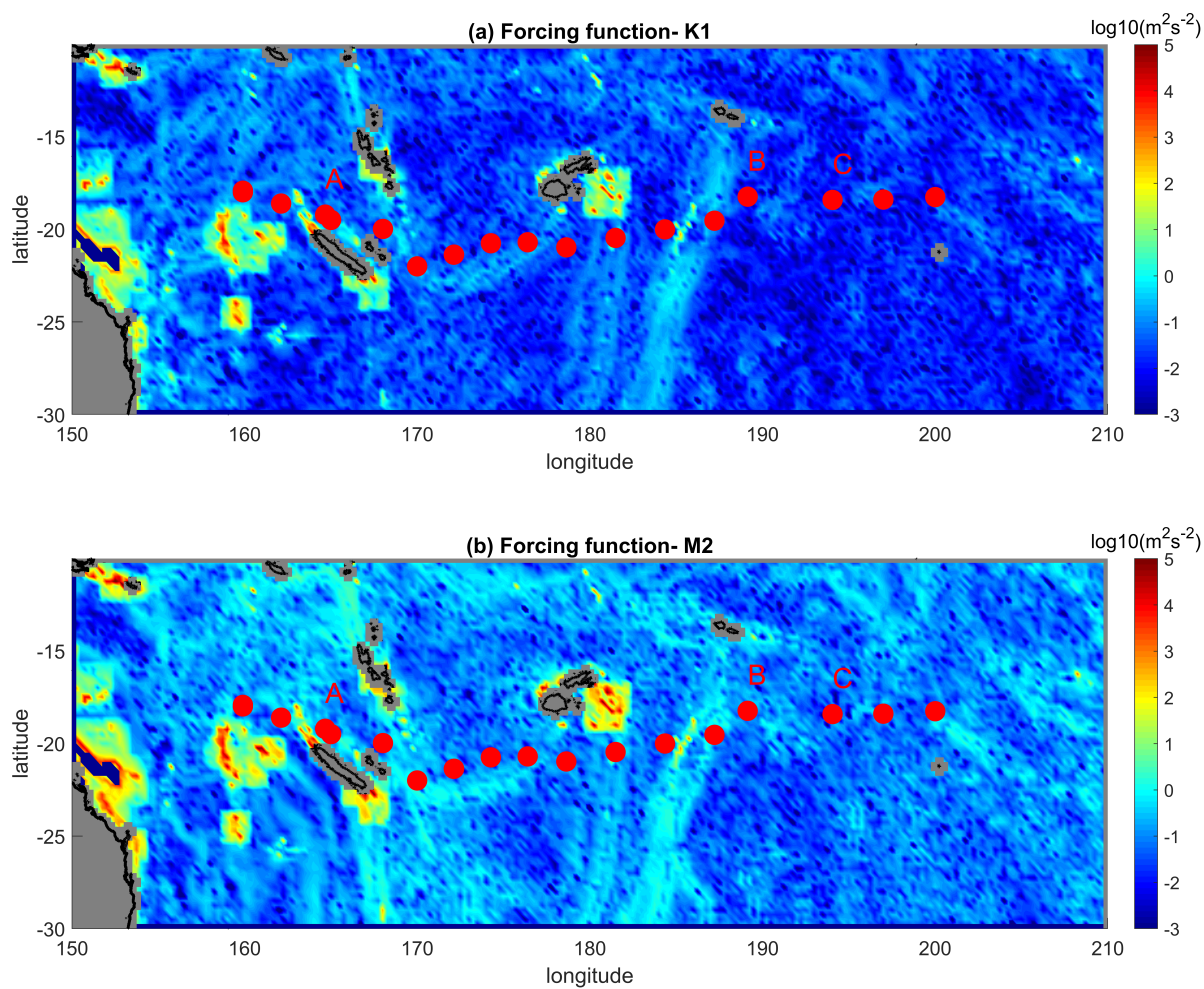
Figure 5. (a) Forcing function for K1 tidal constituent ($\log10(m^2 s^{-2})$); (b) same as in (a) but for M2 tidal constituent. The stations are shown with a red circle and the LD stations are indicated.
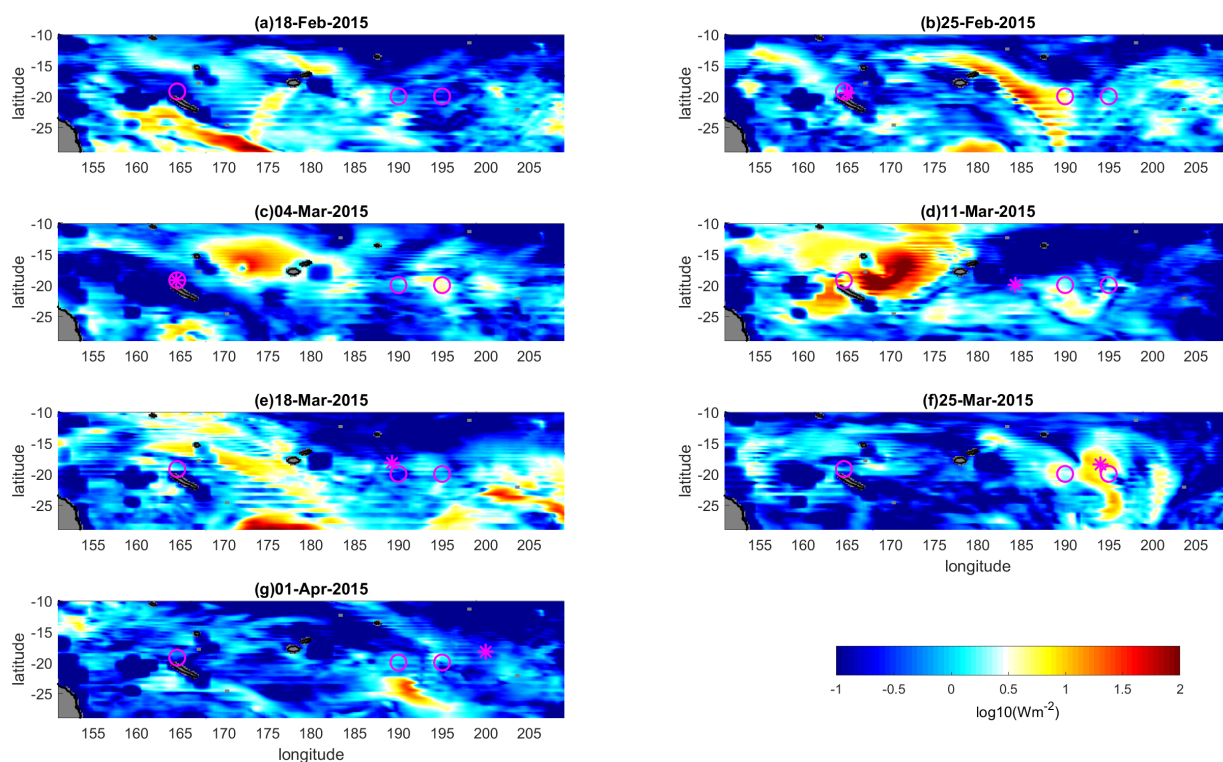
Figure 6. Maps of inertial energy flux (log10($W\,m^{-2}$)) every 7 days during the cruise. Long duration stations are shown with black circles, LD-A was hold during (b) and (c), LD-B during (e) and LD-C during (f). The ship position is displayed with a magenta star and the long duration stations with magenta circles.
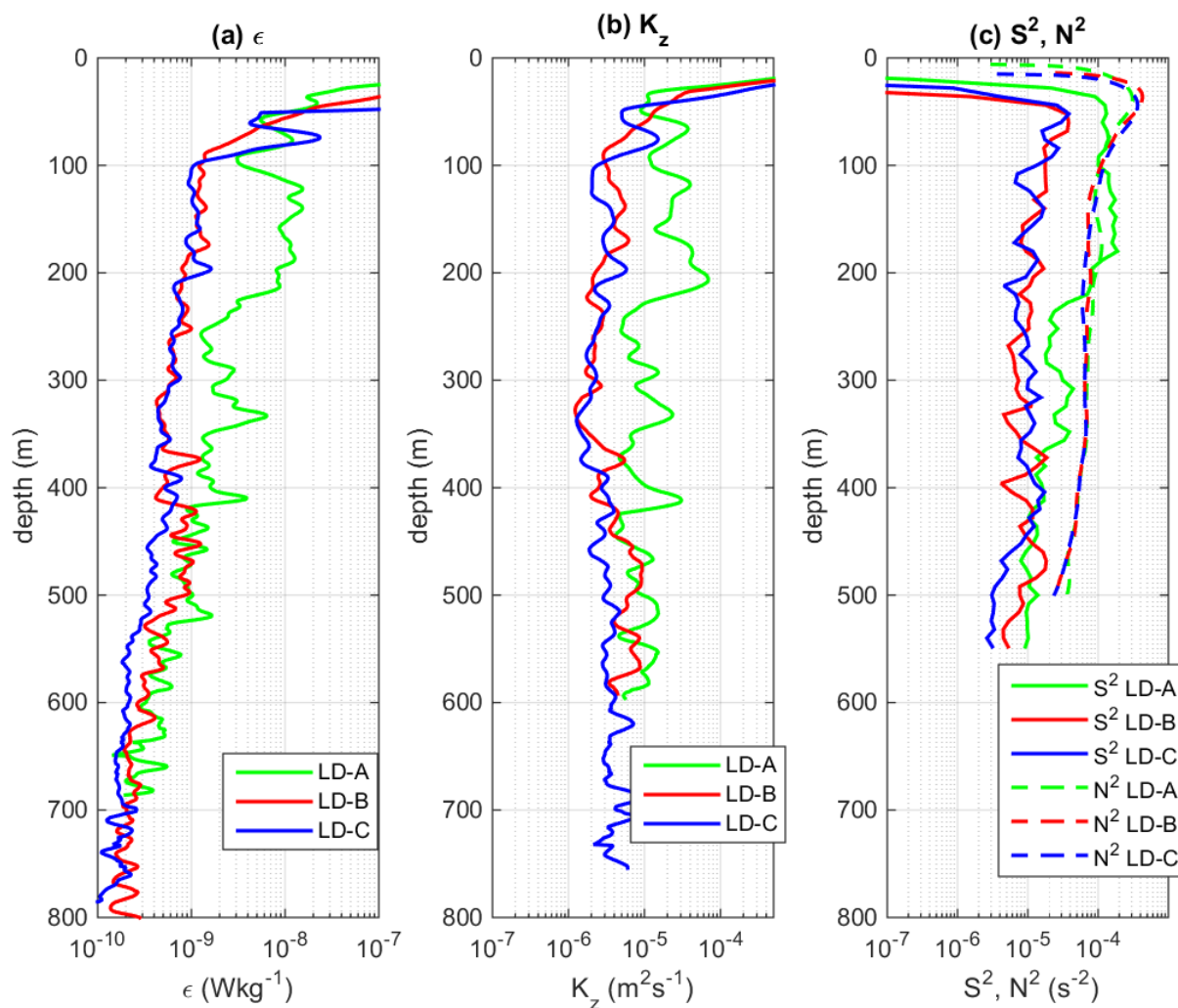
Figure 7. Mean profiles at long durations stations: ϵ in (a), K_z in (b) and S^2 and N^2 in (c). K_z was computed using N from the VMP measurements while the profiles in (c) were inferred from the rosette.
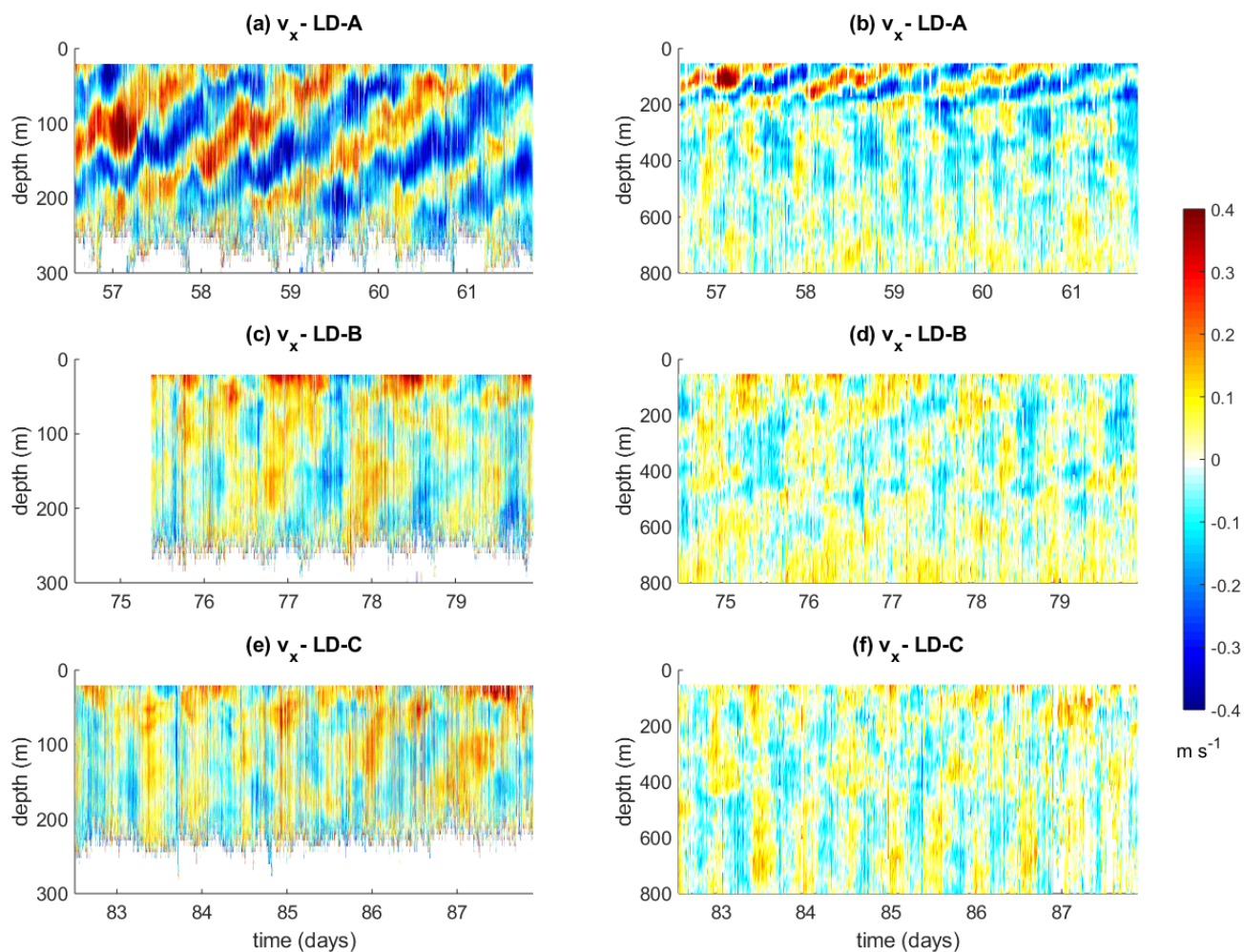
Figure 8. Zonal velocity $(m\,s^{-1})$ as a function of time and depth at the long duration stations, each row from 1 to 3 corresponds to LD-A, LD-B and LD-C respectively, in the first column ship ADCP data from the $150kHz$ instrument down to 300m are displayed and in the second column those from the $38kHz$ instrument down to 800m. Note that in (b) the 150kHz SADCP functionned only a few hours after the beginning of the station sampling.
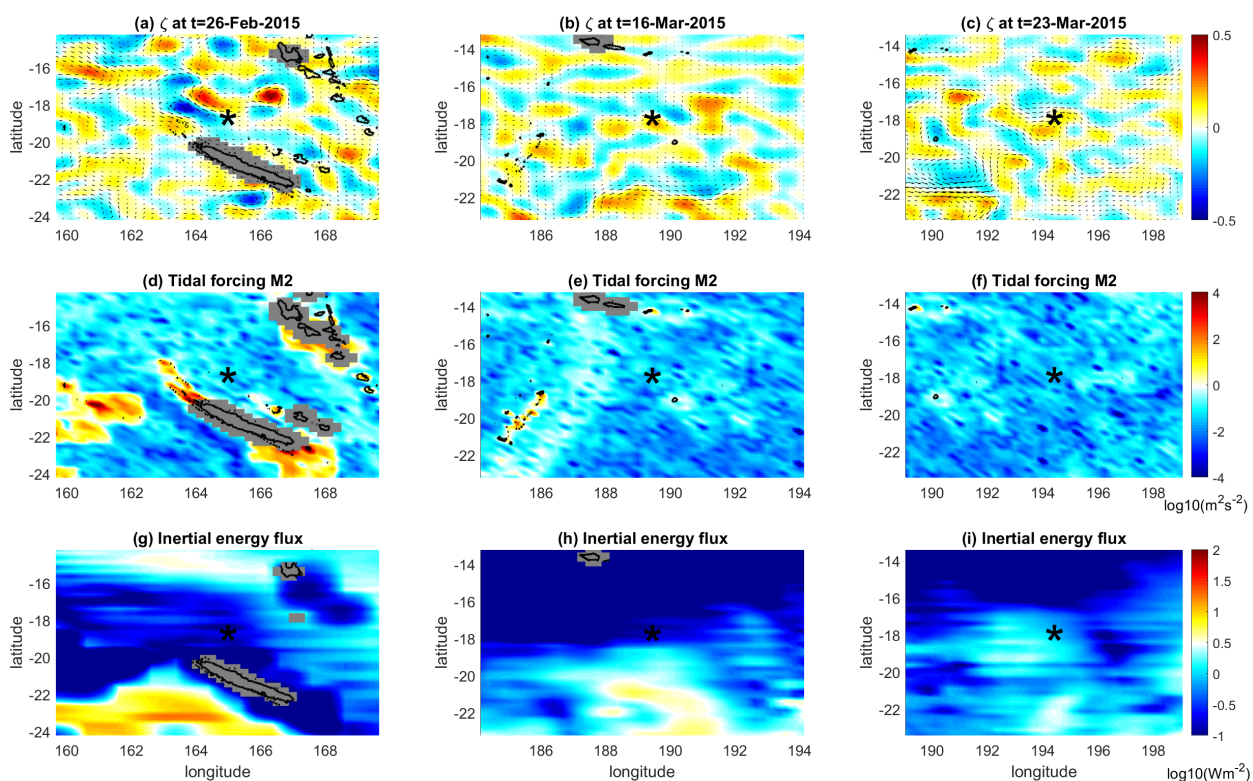
Figure 9. Vorticity inferred from AVISO altimetric data at LD-A (a), LD-B (b) and LD-c (c), non dimensionnalized by the local inertial frequency; M2 tidal generating force at LD-A (d), LD-B (e) and LD-C (f) ($\log10(m^2\,s^{-2})$); Inertial energy flux at LD-A (g), LD-B (h) and LD-C (i) ($\log10(W\,m^{-2})$) one week prior to the beginning of the station.
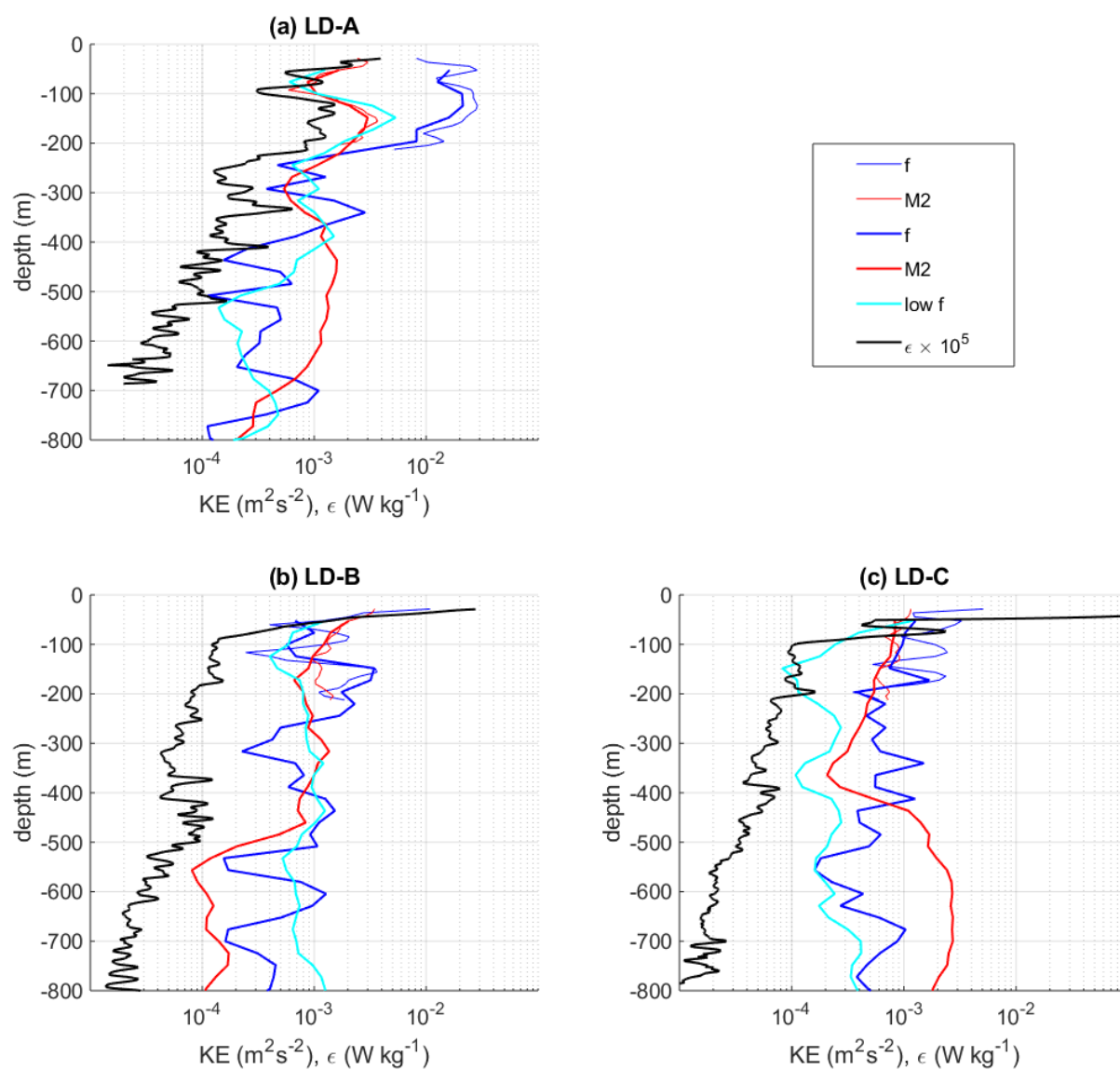
Figure 10. Time-mean profiles of the kinetic energy of the subinertial flow, the inertial and the semi-diurnal frequencies and ϵ at LD-A (a), LD-B (b), and LD-C (c). The kinetic energy was derived from the 38kHz SADCP data but also from the 150kHz SADCP data for the inertial and semi-diurnal kinetic energies (thin blue and red curves).
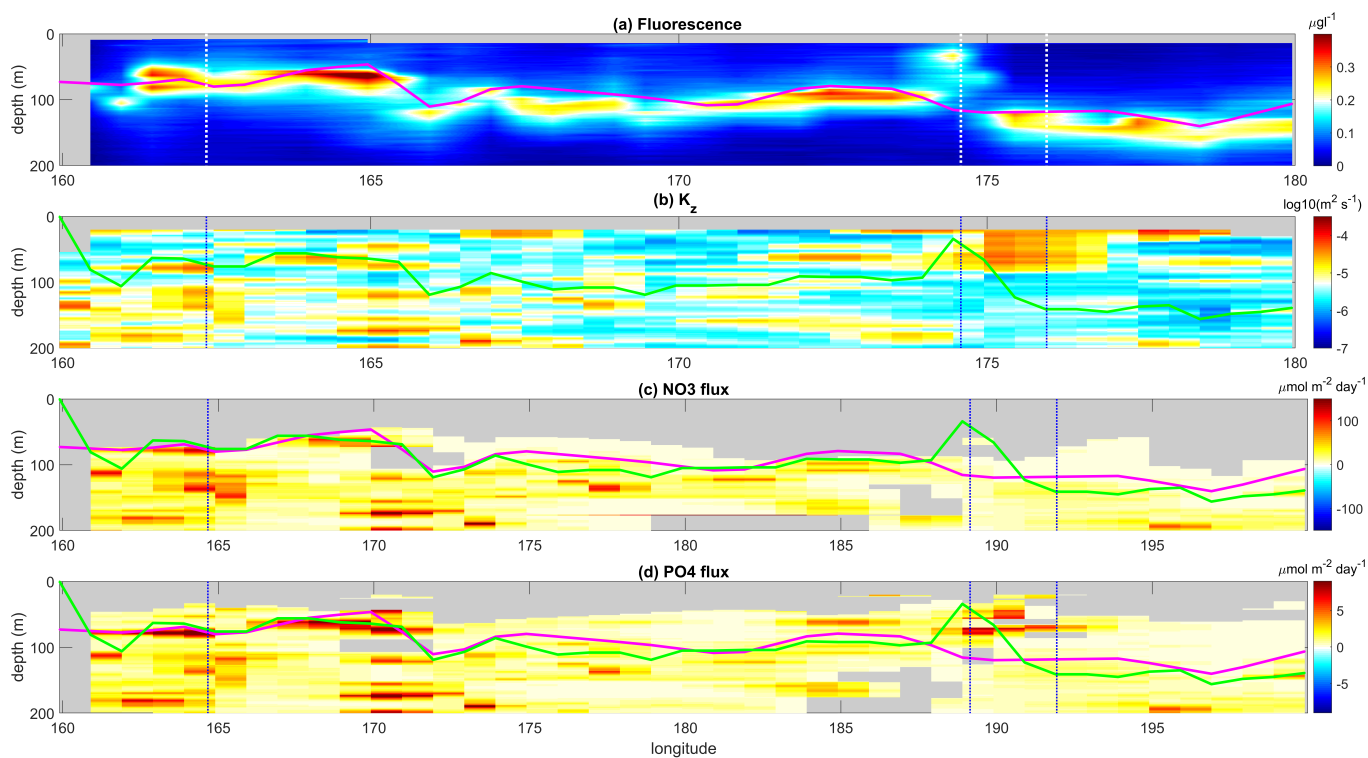
Figure 11. Longitude depth sections of fluorescence, (a), K_z, (b), nitrate turbulent diffusive flux (c) and phosphate turbulent diffusive flux (d). The top of the nitracline is shown with a magenta dotted line and the depth of maximum fluorescence with a green dotted line. The location of the LD stations are shown with a vertical dashed line. The scales of the nitrate and phosphate turbulent diffusive flux are set to match with the typical Redfield ratio in the area (1/16).
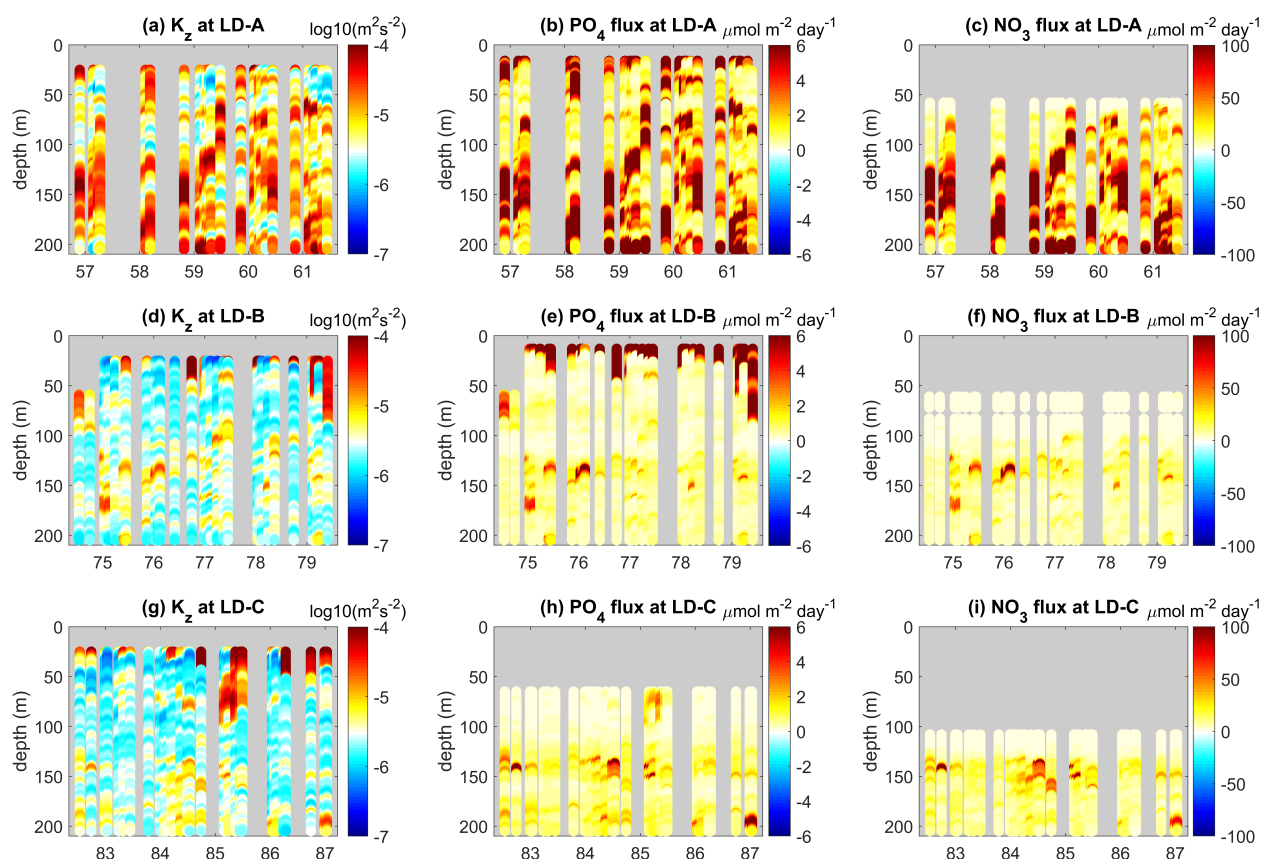
Figure 12. Longitude depth sections of fluorescence, (a), K_z, (b), nitrate turbulent diffusive flux (c) and phosphate turbulent diffusive flux (d). The top of the nitracline is shown with a magenta dotted line and the depth of maximum fluorescence with a green dotted line. The location of the LD stations are shown with a vertical dashed line. The scales of the nitrate and phosphate diffusive flux are set to match with the typical Redfield ratio in the area (1/16).
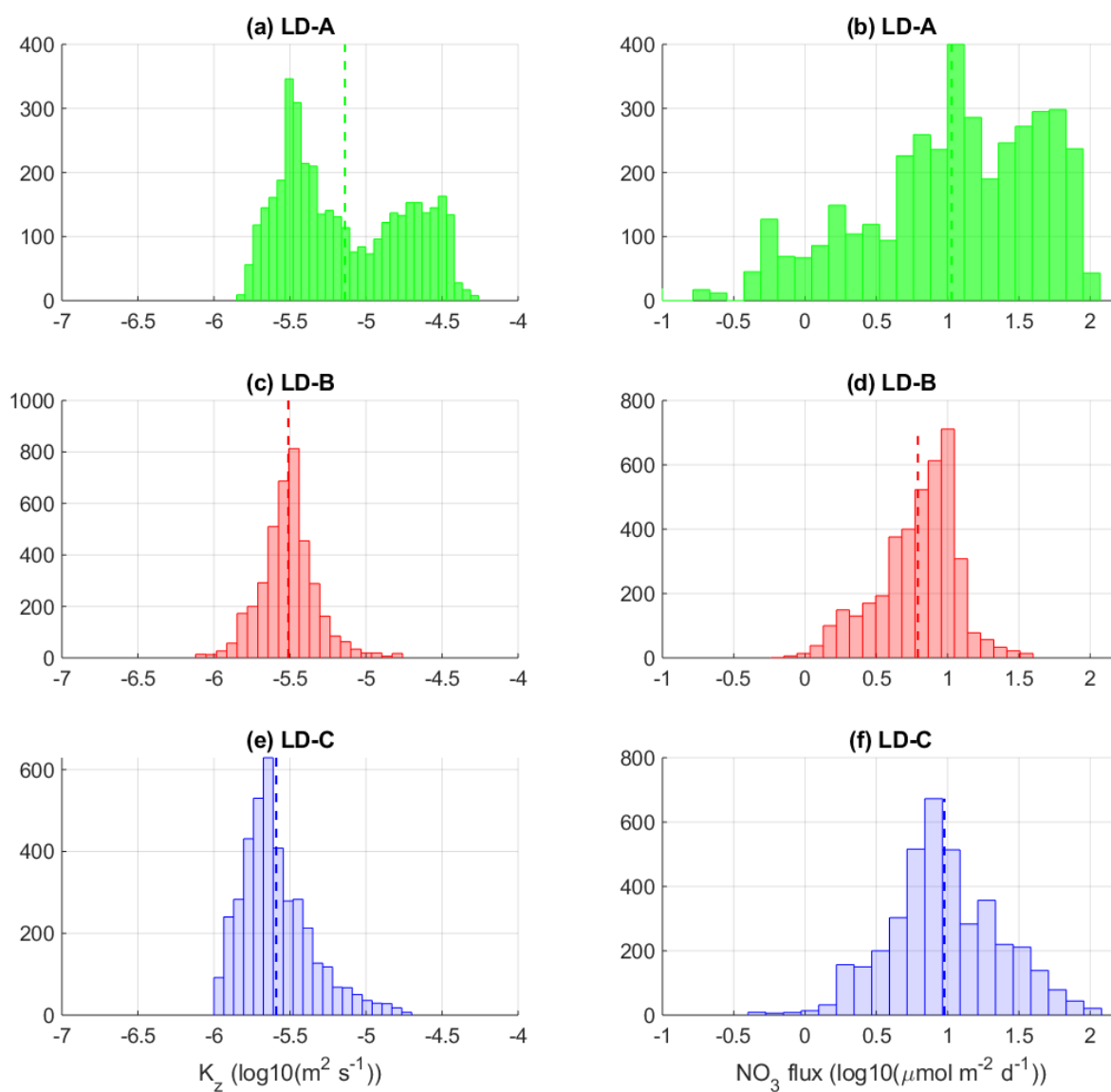
Figure 13. Histograms of K_z (first column) and nitrate turbulent diffusive flux (second column) at long duration stations, LD-A, LD-B and LD-C around the top of the nitracline. The top of the nitracline is defined by the isopycnal, ρ_{NO_3}, with density values taken from Caffin et al. (submitted, this issue), Table 4.
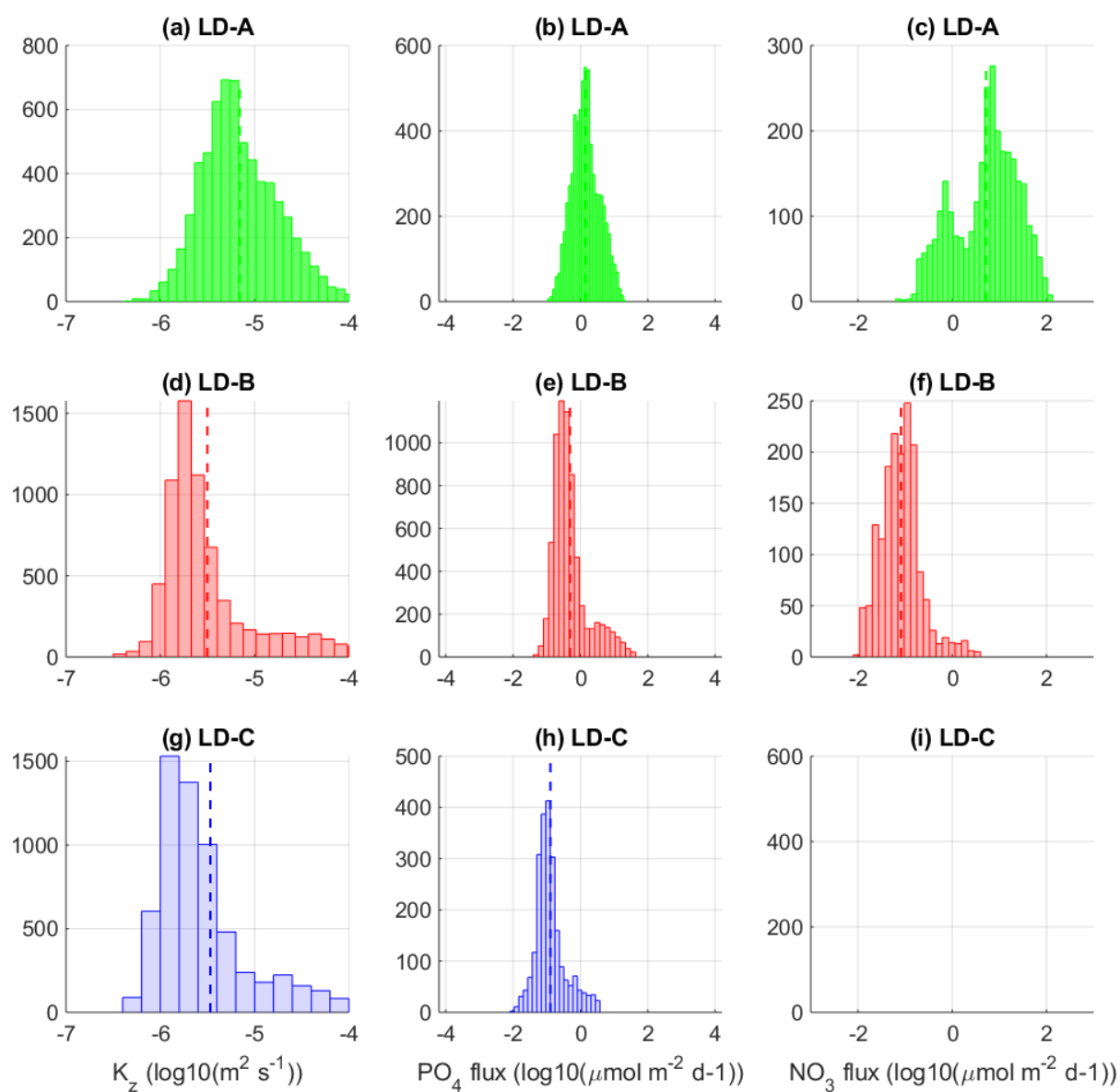
Figure 14. Histograms of K_z (first column), phosphate and nitrate turbulent diffusive fluxes (second and third colums) at long duration stations, LD-A, LD-B and LD-C within the top $[20m; 80m]$. At LD-C the nitrate turbulent diffusive flux is below the noise level within the considered depth interval (i).

Table 1. VMP profiles.

Station	position	depth (m)	number of VMP profiles
SD1	$[159°54.0'E; 18°0.0'S]$	4068	2
SD2	$[162°7.5'E; 18°37.5'S]$	2567	1
SD3	$[164°54'E; 19°19.0'S]$	3252	1
LD-A	$[164°41.28'E; 19°12.78'S]$	3491	30
SD4	$[168°0.0'E; 20°0.0'S]$	4995	1
SD5	$[170°0.0'E; 22°0.0'S]$	4405	1
SD6	$[172°8.0'E; 21°22'S]$	2509	3
SD7	$[174°16'E; 20°44'S]$	2451	2
SD8	$[176°24'E; 20°06'S]$	2028	3
SD9	$[178°39'E; 20°57'S]$	3864	2
SD10	$[178°31'W; 20°28'S]$	819	1
SD11	$[175°40'W; 19°59'S]$	2234	1
SD12	$[172°50'W; 19°29'S]$	7717	1
LD-B	$[170°51.5'W; 18°14.4'S]$	4912	35
SD13	$[169°4.37'W; 18°12.04'S]$	4598	0
LD-C	$[165°45.4'W; 18°40.8'S]$	5277	36